

See discussions, stats, and author profiles for this publication at: <https://www.researchgate.net/publication/228526003>

Euler– Euler Modeling of Flow, Mass Transfer, and Chemical Reaction in a Bubble Column

ARTICLE *in* INDUSTRIAL & ENGINEERING CHEMISTRY RESEARCH · JANUARY 2009

Impact Factor: 2.59 · DOI: 10.1021/ie800233y

CITATIONS

11

READS

60

3 AUTHORS, INCLUDING:



Niels G Deen

Technische Universiteit Eindhoven

175 PUBLICATIONS 3,003 CITATIONS

SEE PROFILE



Hans A. M. Kuipers

Technische Universiteit Eindhoven

436 PUBLICATIONS 9,468 CITATIONS

SEE PROFILE

Euler–Euler Modeling of Flow, Mass Transfer, and Chemical Reaction in a Bubble Column

Dongsheng Zhang, Niels G. Deen,* and J. A. M. Kuipers

Faculty of Science and Technology, Institute of Mechanics Processes and Control Twente (IMPACT), University of Twente, P.O. Box 217, 7500 AE Enschede, The Netherlands

Physical and chemical absorption of pure CO₂ bubbles in water and an aqueous sodium hydroxide (NaOH) solution has been studied in a square cross-sectioned bubble column using the commercial software package CFX-4.4. The subgrid-scale turbulence model of Vreman [*Phys. Fluids* **2004**, *16*, 3670–3681] was employed to evaluate the shear-induced turbulent viscosity in the liquid phase. An “opening” boundary condition was applied at the outlet, whereas the previously studied interfacial coefficients were used in the simulations. Full coupling of fluid flow, mass transfer, and chemical reaction is achieved through the incorporation of a bubble number density equation. The capability of the bubble number density model to predict the bubble size is investigated first. Subsequently, physical absorption of pure CO₂ in water and chemisorption of pure CO₂ bubbles in an aqueous NaOH solution are numerically studied. It was verified for a test case without absorption that the specified bubble size can be reproduced with the aid of a bubble number density equation. For the physical absorption of CO₂ in water, it is found that generally the size of the bubbles in the core of the bubble plume is larger than that of the bubbles trapped in the downflow along the wall. In this test case, the bubble size ranges from 3 to 4 mm. As time proceeds, the differences in bubble size become smaller in both the horizontal and vertical directions. When pure CO₂ is absorbed into an aqueous NaOH solution with an initial pH value of 12, the bubble size does not change very much with time. In this case, the bubble size ranges from 2.7 to 4 mm because the mass-transfer enhancement factor is on the order of unity, as a result of the relatively low pH. The pH history resulting from the numerical model is compared to that obtained from a simple macroscopic model. It is found that numerical results obtained from the case in which the bubble size is solved agree well with the simple model. The observed differences between the simple model and the simulated results obtained with constant bubble size are due to the lack of coupling of mass transfer and fluid flow.

1. Introduction

Bubble column reactors are widely used in chemical, petrochemical, and biological processes. Many processes involve gas–liquid mass transfer with accompanying reactions between the gas and liquid phases themselves or with components dissolved or suspended in them. Despite the widespread application of bubble columns and intensive research efforts devoted to understanding their complex behavior, detailed knowledge on the fluid flow, mass transfer, and chemical reactions as well as their interactions is currently limited.

Experimental investigation and numerical simulations are widely used to study and analyze gas–liquid flow processes. In the last 2 decades, two approaches were frequently used to simulate the flow in bubble columns: the Euler–Euler (E–E) model^{2–5} and the Euler–Lagrange (E–L) model.^{6–8} Detailed descriptions of the E–L and E–E models are found in previous studies.^{3,8,9} Figure 1 schematically shows how the two models account for the bubble shrinkage due to physical absorption or chemisorption. In the E–L approach, bubble shrinkage can be monitored for each individual bubble, while accounting for the properties of the individual bubbles. In the E–E approach, detailed information of the bubble size distribution can be obtained by solving an additional equation, which accounts for the breakage and coalescence of bubbles as well as the growth or shrinkage of bubbles due to mass transfer. The MUSIG (multiple size group) model,¹⁰ the interfacial area concentration,^{11–14} and the recently developed S_g model¹⁵ were found to track the

bubble size distribution, which will be discussed later. Though it is easier to track the bubble size change in the E–L model, it is less suited to study gas–liquid flow in large-scale bubble columns or at high gas holdup because of its high computational effort and memory requirement. It is noted here that, specifically for gas–liquid systems in the homogeneous flow regime, the E–E and E–L models give similar results. In this study, the E–E model is adopted to investigate mass transfer in bubbly flows.

When a chemical reaction is considered in a gas–liquid system, the interactions between the prevailing processes are very complex, as is schematically depicted in Figure 2: the chemical reaction rate depends on the local concentration of the species, which is determined by the interphase mass-transfer process and the mixing induced by the dispersed bubbles. The interphase mass-transfer rate depends on the mass-transfer

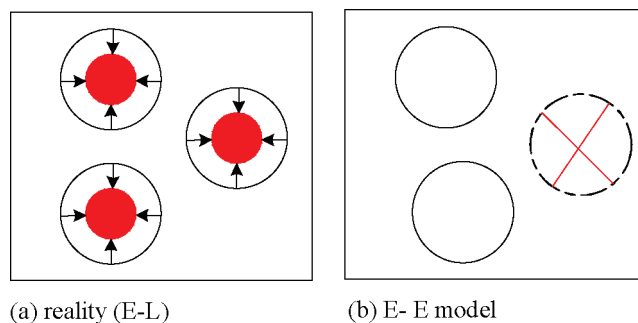


Figure 1. Schematic illustration of bubble shrinkage treatment due to mass transfer in the E–E and E–L models.

* To whom correspondence should be addressed. Tel: +31-53-489 4138. Fax: +31-53-489 2882. E-mail: N.G.Deen@utwente.nl.

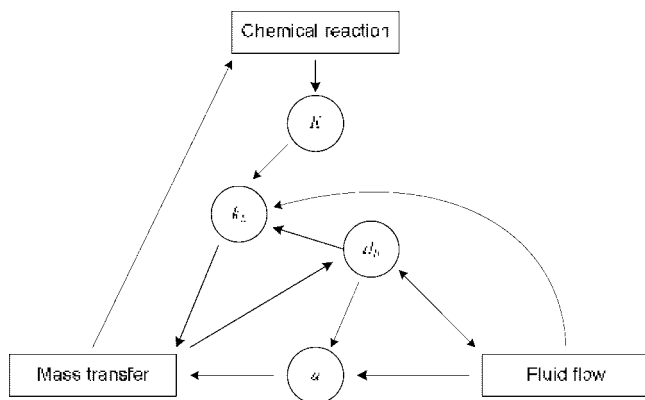


Figure 2. Schematic representation of the interdependency of fluid flow, mass transfer, and chemical reaction.

Table 1. Source Terms Used in the Species Transport Equations

species	source ($\text{kg m}^{-3} \text{s}^{-1}$)
$\text{CO}_2(\text{aq})$	$\dot{m}_{\text{G} \rightarrow \text{L}} + \alpha(R_{12} - R_{11})M_{\text{CO}_2}$
OH^-	$\alpha_{\text{L}}(R_{12} - R_{11} + R_{22} - R_{21})M_{\text{OH}^-}$
HCO_3^-	$\alpha_{\text{L}}(R_{12} - R_{11} + R_{22} - R_{21})M_{\text{HCO}_3^-}$
CO_3^{2-}	$\alpha_{\text{L}}(R_{21} - R_{22})M_{\text{CO}_3^{2-}}$
CO_2	$-\dot{m}_{\text{G} \rightarrow \text{L}}$

Table 2. Case Definition and Involved Parameters^a

case	liquid	initial pH	inlet gas	d_{B}	C_{D}	species equation
1	pure water	7	air	4 mm	1.071	no
2	pure water	7	pure CO_2	4 mm	Tomiyama ³⁴	yes
3	pure water	7	pure CO_2	eq 29	Tomiyama ³⁴	yes
4	NaOH solution	12	pure CO_2	4 mm	Tomiyama ³⁴	yes
5	NaOH solution	12	pure CO_2	eq 29	Tomiyama ³⁴	yes

^a $\rho_{\text{L}} = 1000 \text{ kg m}^{-3}$, $\mu_{\text{L,Lam}} = 0.001 \text{ kg m}^{-1} \text{s}^{-1}$, $\rho_{\text{G}} = 1.98 \text{ kg m}^{-3}$, $\mu_{\text{L,Lam}} = 1.812 \times 10^{-5} \text{ kg m}^{-1} \text{s}^{-1}$, $\sigma = 0.07275 \text{ N m}^{-1}$, $D_{\text{CO}_2} = 1.699 \times 10^{-9} \text{ m}^2 \text{s}^{-1}$, $D_{\text{OH}^-} = 5.3 \times 10^{-9} \text{ m}^2 \text{s}^{-1}$, $D_{\text{HCO}_3^-} = 1.1 \times 10^{-9} \text{ m}^2 \text{s}^{-1}$, and $D_{\text{CO}_3^{2-}} = 1.5 \times 10^{-9} \text{ m}^2 \text{s}^{-1}$.

coefficient, the interfacial area concentration, and the chemical reaction rate. Meanwhile, the mass-transfer coefficient is a function of the local hydrodynamics, which itself is influenced by the bubble shrinkage due to physical or chemical absorption and variation of physical properties due to the inhomogeneous distributions of the chemical species. These complex interactions make the overall prediction of the performance and scale-up of this kind of reactor very difficult.

Because of the complexity of gas–liquid systems, some researchers have simplified the modeling in the E–E approach to steady-state conditions or adopted one- or two-dimensional models.^{16–18} The so-called hybrid method is used as well to solve these kinds of problems, in which computational fluid dynamics (CFD) is employed only for the simulation of hydrodynamics, and the chemical reactions are accounted for by a custom-built compartment model.^{19–21} Though the model of Fleischer et al.¹⁶ is capable of qualitatively predicting the transient behavior of a chemisorption process in a slender bubble column, many authors^{2,3,8,9} found that bubble columns exhibit inherently unsteady three-dimensional flow characteristics. In the so-called hybrid model, the interactions between hydrodynamics, mass transfer, and chemical reactions are decoupled; each subproblem is solved with a separate model, and consequently, the interaction among hydrodynamics, mass-transfer, and chemical reaction processes is not necessarily accounted for. Furthermore, the influence of the mass transfer and chemical reaction on the hydrodynamics is not accounted for, and because

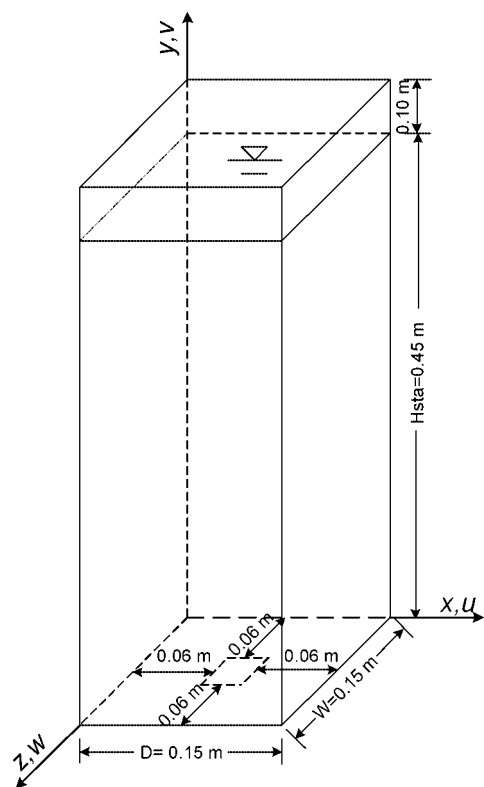


Figure 3. Schematic representation of the investigated bubble column.

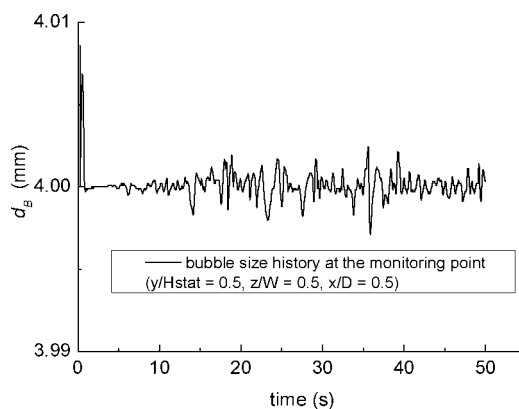


Figure 4. Local bubble diameter history obtained for case 1.

of limitations in representing a change in the bubble size, the predictive capabilities will be limited.

In the E–E model, full coupling of mass transfer, fluid flow, and chemical reaction can be achieved when the local bubble size distribution is known. Though the MUSIG model¹⁰ is capable of predicting a bubble size distribution, its considerable computational effort constrains its application to small-scale geometries. That is, to get a reliable bubble size distribution, typically 20 bubble size classes are required in the MUSIG approach, which considerably increases the computational cost of the simulations. As was found in previous studies,⁹ interfacial transfer terms appear in each of the conservation equations of mass, momentum, and species in each phase. The interfacial transfer terms are strongly related to the interfacial area concentration, a , and the local transfer mechanisms such as the degree of turbulence near the interfaces. This makes the interfacial area concentration a very important quantity. Hence, it was pointed out by Ishii²³ that accurate modeling of the local interfacial area concentration is the first step to be taken for the

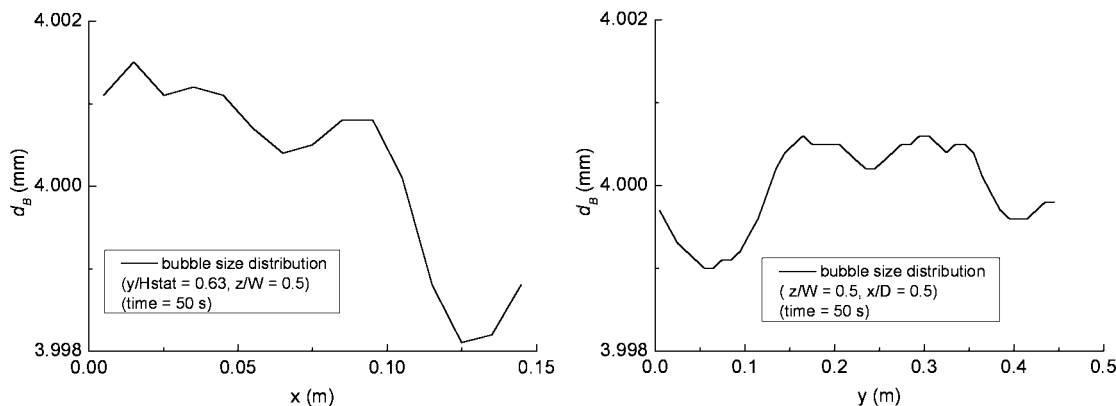


Figure 5. Instantaneous bubble Sauter diameter distribution in horizontal (left) and vertical (right) directions, obtained for case 1.

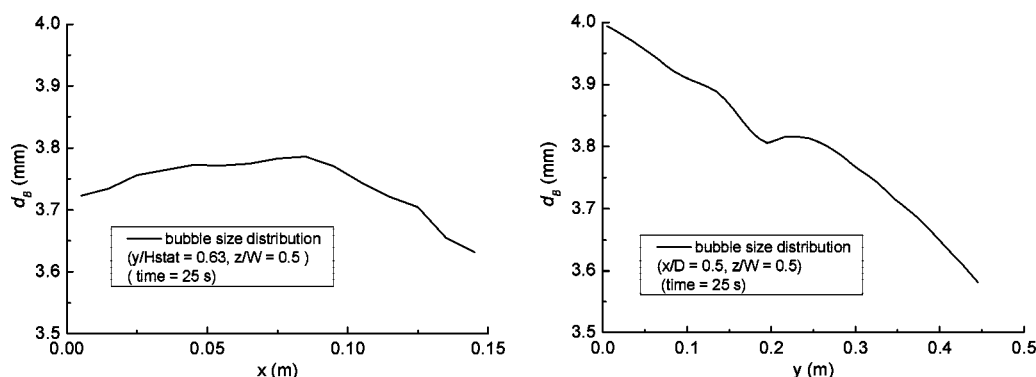


Figure 6. Instantaneous bubble size distribution in horizontal (left) and vertical (right) directions during physical absorption of pure CO_2 in water (case 3).

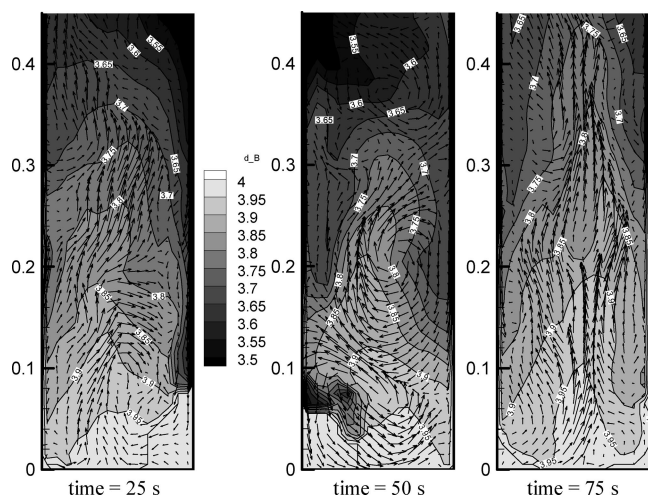


Figure 7. Snapshots of the instantaneous bubble diameter distribution and liquid-phase velocity field in the plane of $z/W = 0.5$ obtained from numerical simulation during physical absorption of pure CO_2 in water at different times (case 3).

development of reliable two-fluid (E–E) model closure relations. In the past 2 decades, much attention^{11–15,24–28} has been concentrated toward developing an interfacial area concentration transport equation to describe the temporal and spatial evolution of the two-phase geometrical structure. The local Sauter mean diameter d_{32} is obtained through local gas holdup, α_G , and interfacial area concentration, a . The main differences among the aforementioned interfacial area concentration models are the closures for breakup and coalescence. Furthermore, the transport equation of the interfacial area concentration can be easily transformed to the bubble number density equation, as

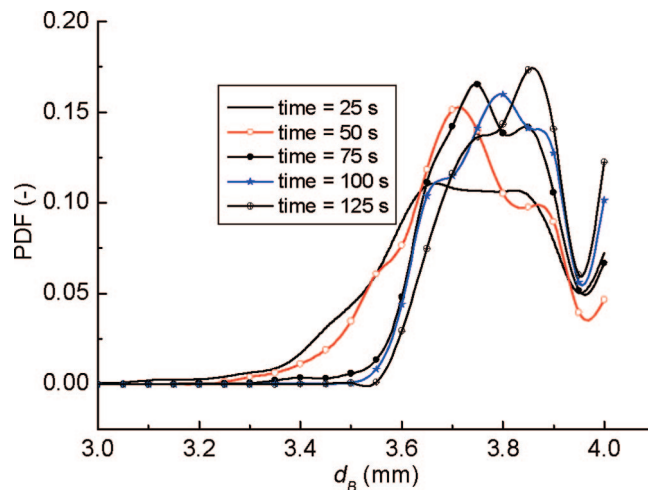


Figure 8. Probability density function of the bubble size in the entire column at different times (case 3).

found in the work of Yeoh and Tu.²⁹ It is more straightforward to use the bubble number density to track the bubble size because the bubble number is not changed as a result of mass transfer, which makes the bubble number density a passive scalar. Therefore, it is adopted in the current work.

The chemisorption of CO_2 into an aqueous NaOH solution is chosen as the test case for this work because it exhibits all important phenomena encountered in practice while its reaction mechanism is well understood and the reaction kinetics are well established.

In this work, simulations were performed with the use of a E–E model for the flow with mass transfer and chemical reaction in a square cross-sectioned gas–liquid bubble column

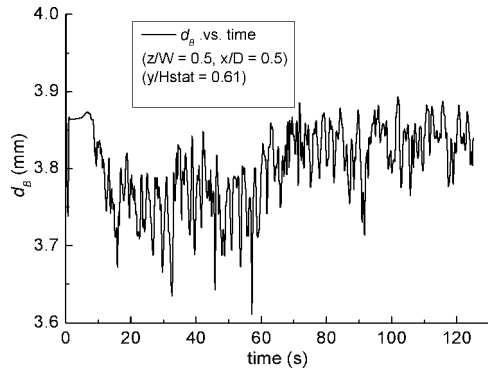


Figure 9. Local bubble diameter history obtained from numerical simulation during physical absorption of pure CO₂ in water (case 3).

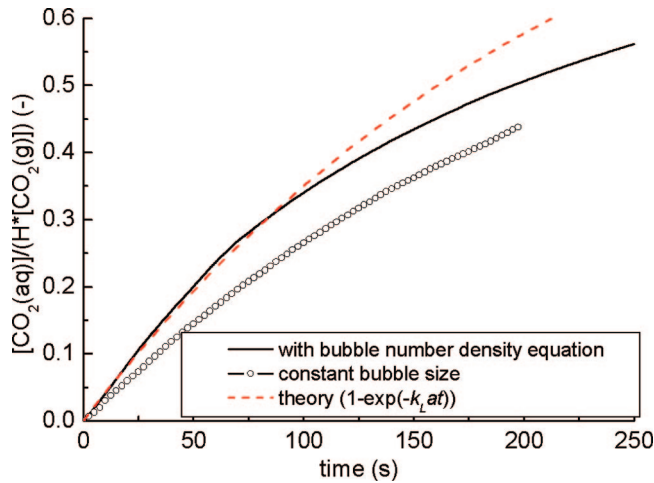


Figure 10. Comparison of the normalized dissolved CO₂ concentration in the entire column obtained from different cases during physical absorption of pure CO₂ in water (cases 2 and 3).

($W \times D \times H = 0.15 \times 0.15 \times 0.55 \text{ m}^3$) that is aerated with pure CO₂ gas through the bottom plane with a superficial gas velocity of $V_s = 0.005 \text{ m s}^{-1}$. Drag, virtual mass, and lift forces are considered for the interfacial momentum transfer. The subgrid-scale (SGS) turbulence model proposed by Vreman¹ was employed to evaluate the shear-induced turbulent viscosity in the continuous phase. Specifically, we study the feasibility and applicability of the bubble number density equation for the numerical simulation of the fully coupled mass transfer, fluid flow, and chemical reaction in a reactive gas–liquid flow. Chemisorption of CO₂ into aqueous NaOH solutions with an initial pH value of 12 is studied.

2. Governing Equations

The equations of the two-fluid model can be obtained by volume-averaging of the local instantaneous equations for single-phase flow.³⁰ Two sets of balance equations for mass and momentum are obtained. The generic conservation equations for mass and momentum respectively take the following form:

$$\frac{\partial(\alpha_k \rho_k)}{\partial t} + \nabla \cdot (\alpha_k \rho_k \mathbf{u}_k) = -\dot{m}_{k \rightarrow l} \quad (1)$$

$$\frac{\partial(\alpha_k \rho_k \mathbf{u}_k)}{\partial t} + \nabla \cdot (\alpha_k \rho_k \mathbf{u}_k \mathbf{u}_k + \alpha_k \tau_k) = \alpha_k \rho_k \mathbf{g} - \alpha_k \nabla p + \mathbf{M}_k - \dot{m}_{k \rightarrow l} \mathbf{u}_k \quad (2)$$

where the index k refers to the phase under consideration (L for liquid and G for gas) and l to the other phase. $\mathbf{u} = (u, v, w)$

is the velocity vector. The volume fraction of each phase is denoted by α , whereas $\dot{m}_{k \rightarrow l}$ is the mass-transfer rate from phase k to phase l . \mathbf{M}_k represents the interphase momentum exchange between phase k and all other phases and accounts for the interface forces.

For phase k , the stress tensor τ_k appearing in eq 2 reads

$$\tau_k = -\mu_{k,\text{eff}} \left(\nabla \mathbf{u}_k + (\nabla \mathbf{u}_k)^T - \frac{2}{3} \nabla \cdot \mathbf{u}_k \right) \quad (3)$$

$\mu_{k,\text{eff}}$ is the effective viscosity for phase k . For the liquid phase ($k = L$), it is composed of three contributions: the molecular viscosity $\mu_{L,\text{Lam}}$, the shear-induced turbulent viscosity $\mu_{L,\text{Tur}}$, and an extra term due to bubble-induced turbulence μ_{BIT} :

$$\mu_{L,\text{eff}} = \mu_{L,\text{Lam}} + \mu_{L,\text{Tur}} + \mu_{\text{BIT}} \quad (4)$$

The effective viscosity of the gas phase ($k = G$) is calculated as follows:³¹

$$\mu_{G,\text{eff}} = \frac{\rho_G}{\rho_L} \mu_{L,\text{eff}} \quad (5)$$

In this work, the liquid-phase shear-induced turbulent viscosity is evaluated by the SGS model proposed by Vreman:¹

$$\mu_{L,\text{Tur}} = 2.5 \rho_L C_s^2 \sqrt{\frac{B_\beta}{S_{ij} S_{ij}}} \quad (6)$$

where $B_\beta = \beta_{11}\beta_{22} - \beta_{12}^2 + \beta_{11}\beta_{33} - \beta_{13}^2 + \beta_{22}\beta_{33} - \beta_{23}^2$, $S_{ij} = \partial u_i / \partial x_j$, $\beta_{ij} = \Delta_i^2 S_{mi} S_{mj}$, and Δ_i is the filter width in the i^{th} direction. C_s is a model constant, and $C_s = 0.1$ is used based on the findings in the previous study.^{9,32}

The bubble-induced turbulent viscosity appearing in eq 4 is accounted for through the model of Sato and Sekoguchi:³³

$$\mu_{\text{BIT}} = \rho_L \alpha_G C_{\mu,\text{BIT}} d_B |\mathbf{u}_G - \mathbf{u}_L| \quad (7)$$

where $C_{\mu,\text{BIT}}$ is a model constant that is set to 0.6.

When we assume that there is no coalescence and breakup, the bubble number density equation is given by

$$\frac{\partial n}{\partial t} + \nabla \cdot (\mathbf{u}_g n) = 0 \quad (8)$$

The Sauter mean diameter can be obtained from the bubble number density and the local gas fraction and is expressed as

$$d_{32} = \left(\frac{6\alpha_G}{\pi n} \right)^{1/3} \quad (9)$$

In this work, only homogeneous gas–liquid flows are considered. Hence, it is safe to assume that coalescence and breakup can be neglected. As a result, the bubble size is only changed as a result of mass transfer. Assuming that locally (i.e., at the level of grid cells) the changes in the bubble size are the same for all bubbles in the control volume, it is allowable to characterize the bubble size with the zeroth moment of the bubble size distribution, i.e., the local mean bubble size.

If one was to apply the proposed model to heterogeneous flow regimes, clearly the assumptions made are no longer valid. That is, coalescence and breakup are significant and locally there will be a broad bubble size distribution. In that case, it would be worthwhile to consider multiple classes, for instance, small bubbles and bubbles, each with a varying local mean bubble size. The bubble density equation model might also be extended by tracking higher order moments to better describe the bubble size distribution (also see the work of Bove et al.³⁴ and Dorao and Jakobsen³⁵ and the references cited therein).

The term \mathbf{M}_k in eq 2, describing the interface forces, is given by the following expression:

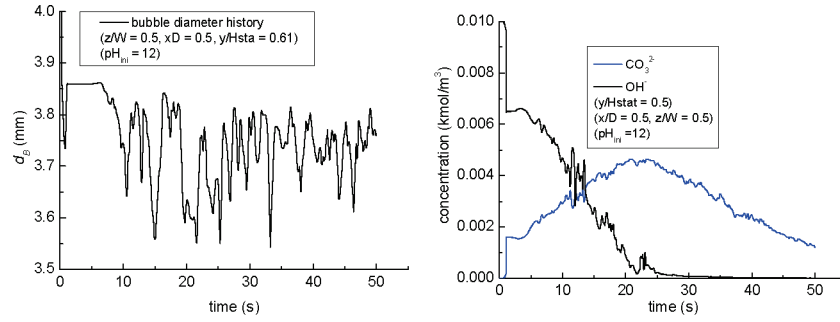


Figure 11. Local bubble diameter (left) and concentration history of CO_3^{2-} and OH^- species (right) evolution history obtained from numerical simulation during chemisorption of pure CO_2 in an aqueous NaOH solution with an initial pH of 12. A bubble number density equation is used to obtain the bubble size (case 5).

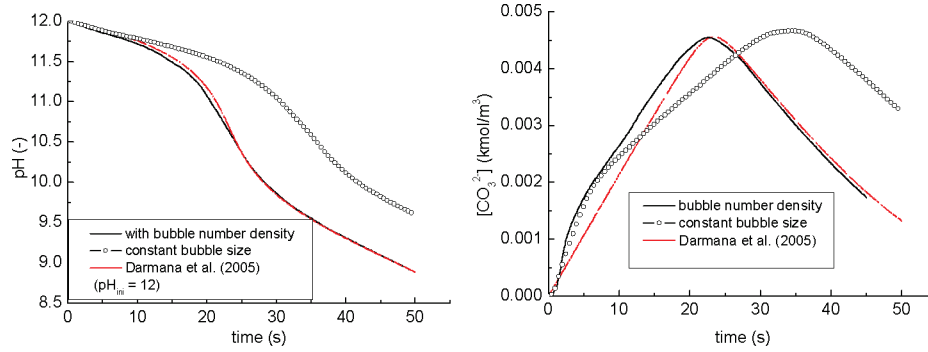


Figure 12. Comparison of the overall pH history (left) and concentration history of the CO_3^{2-} species (right) in the entire column involved in the chemical reaction process resulting from different numerical simulations (cases 4 and 5).

$$\mathbf{M}_L = -\mathbf{M}_G = \mathbf{M}_{L,D} + \mathbf{M}_{L,L} + \mathbf{M}_{L,VM} \quad (10)$$

where the terms on the right-hand side represent forces due to drag, lift, and virtual mass, respectively. They are calculated as

$$\mathbf{M}_{L,D} = \frac{3}{4} \alpha_G \rho_L \frac{C_D}{d_B} |\mathbf{u}_G - \mathbf{u}_L| (\mathbf{u}_G - \mathbf{u}_L) \quad (11)$$

$$\mathbf{M}_{L,L} = \alpha_G \rho_L C_L (\mathbf{u}_G - \mathbf{u}_L) \times \nabla \times \mathbf{u}_L \quad (12)$$

$$\mathbf{M}_{L,VM} = \alpha_G \rho_L C_{VM} \left(\frac{D_G \mathbf{u}_G}{Dt} - \frac{D_L \mathbf{u}_L}{Dt} \right) \quad (13)$$

According to Tomiyama,³⁶ the virtual mass coefficient vector \mathbf{C}_{VM} takes the form $(C_{VM,h}, C_{VM,v}, C_{VM,h})$. On the basis of our previous study,⁹ the following interfacial coefficients are used in this work:

$$C_L = 0.5 \quad (14)$$

$$C_{VM,h} = \frac{E_b \cos^{-1} E_b - \sqrt{1 - E_b^2}}{E_b^2 \sqrt{1 - E_b^2} - E_b \cos^{-1} E_b}$$

$$C_{VM,v} = \frac{\cos^{-1} E_b - E_b \sqrt{1 - E_b^2}}{(2E_b - 1 - E_b) \sqrt{1 - E_b^2} - \cos^{-1} E_b} \quad (15)$$

where E_b is the bubble aspect ratio. According to numerical results obtained with a front tracking model,³⁷ it takes a value of $E_b = 0.375$.

When the bubble size is changing, the drag coefficient is modeled with the correlation of Tomiyama:³⁶

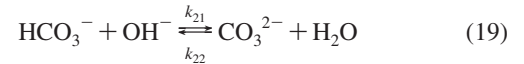
$$C_D = \max \left[\min \left[\frac{16}{Re} (1 + 0.15 Re^{0.687}), \frac{16}{Re} \right], \frac{8}{3} \frac{E\ddot{o}}{E\ddot{o} + 4} \right] \quad (16)$$

The chemisorption of CO_2 in aqueous alkaline solutions takes place via two reactions. Before these reactions take place, CO_2

gas is transferred to the liquid phase through physical absorption:



Subsequently, the elementary reactions then proceed as follows:



where k_{11} and k_{12} respectively are the forward and backward rate constants for the first reaction (eq 18) and k_{21} and k_{22} represent the forward and backward rate constants for the second reaction (eq 19). The reaction rates are consequently written as follows:

$$R_{11} = k_{11} [\text{CO}_2(\text{aq})] [\text{OH}^-] \quad (20)$$

$$R_{12} = k_{12} [\text{HCO}_3^-] \quad (21)$$

$$R_{21} = k_{21} [\text{HCO}_3^-] [\text{OH}^-] \quad (22)$$

$$R_{22} = k_{22} [\text{CO}_3^{2-}] \quad (23)$$

The expressions for the rate constants are provided in Appendix A.

The mass fraction of a chemical species A in the liquid mixture is represented by Y_L^A . The chemical species transport equations for the liquid phase are given by

$$\frac{\partial (\alpha_L \rho_L Y_L^A)}{\partial t} + \nabla \cdot (\alpha_L \rho_L \mathbf{u}_L Y_L^A - \alpha_L \Gamma_L^A \nabla Y_L^A) = S_A \quad (24)$$

whereas the gas-phase transport equation for CO_2 is given by

$$\frac{\partial(\alpha_G \rho_G Y_G^{\text{CO}_2})}{\partial t} + \nabla \cdot (\alpha_G \rho_G \mathbf{u}_G Y_G^{\text{CO}_2} - \alpha_G \Gamma_G^{\text{CO}_2} \nabla Y_G^{\text{CO}_2}) = S_G^{\text{CO}_2} \quad (25)$$

The relevant chemical species and their source terms are listed in Table 1.

The mass-transfer rate of species CO_2 per unit volume, $\dot{m}_{G \rightarrow L}$, from the dispersed phase to the continuous phase is defined as

$$\dot{m}_{G \rightarrow L} = k_L a E \rho_L (Y_{GL,e}^{\text{CO}_2} - Y_L^{\text{CO}_2}) \quad (26)$$

where k_L is the overall mass-transfer coefficient for the chemical species $\text{CO}_2(\text{aq})$, $a = 6\alpha_G/d_{32}$ is the interfacial area concentra-

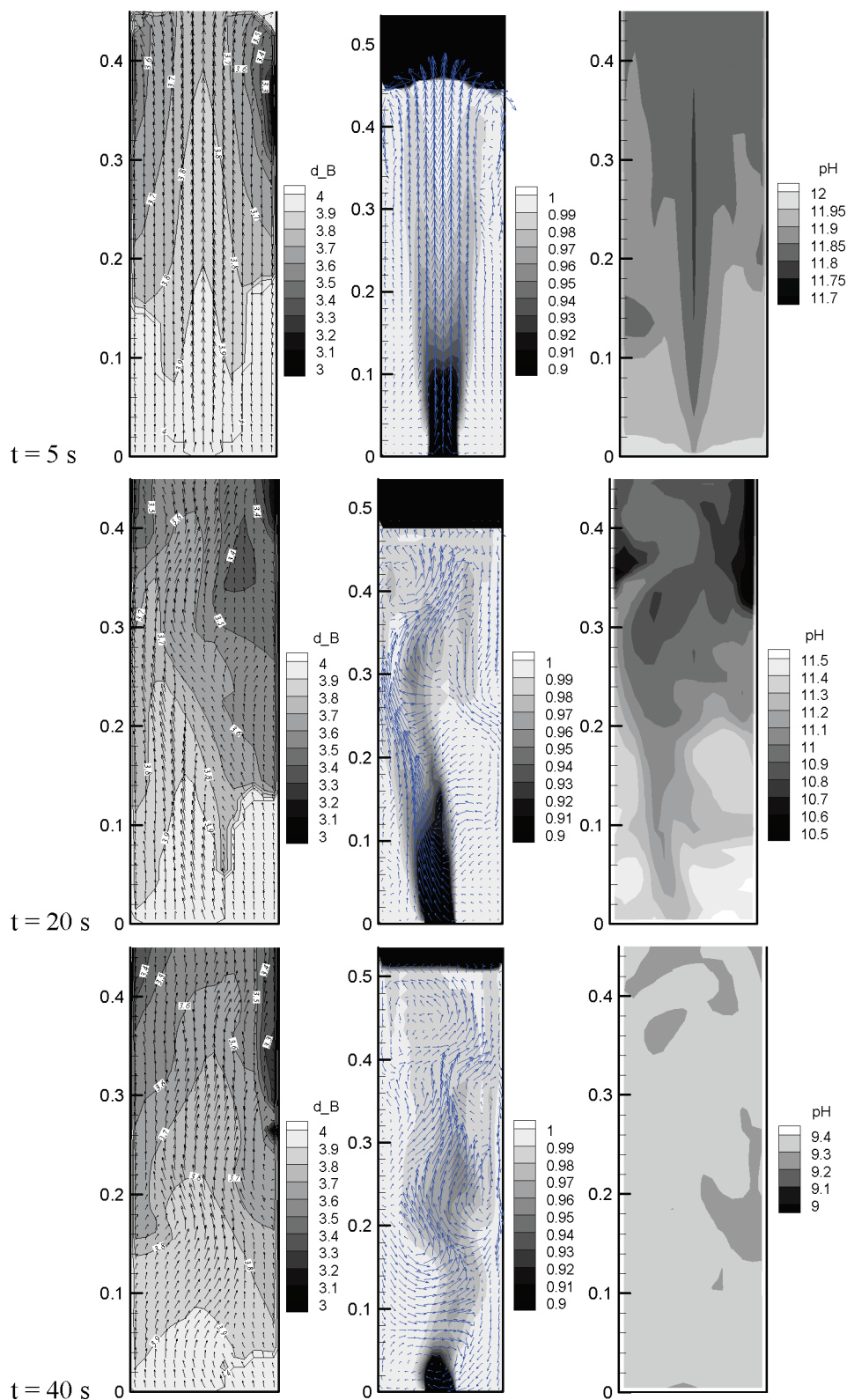


Figure 13. Snapshots of instantaneous bubble size distribution and gas-phase velocity field (left), liquid-phase volume fraction, and velocity field (middle) and pH distribution (right) in the plane of $z/W = 0.5$ at different times during chemisorption of pure CO_2 in an aqueous NaOH solution with an initial pH of 12 (case 5).

tion, E is the enhancement factor due to the chemical reaction, and $Y_{GL,e}^{CO_2}$ is the equilibrium mass fraction of $CO_2(aq)$ in the liquid phase, which is determined by Henry's law:

$$Y_{GL,e}^{CO_2} = H^{CO_2} Y_G^{CO_2} \frac{\rho_G}{\rho_L} \quad (27)$$

Note that eqs 26 and 27 differ somewhat from the usual formulation in terms of concentration. The latter can simply be retained by replacing the mass concentration ($\rho_L Y^A$) of component A by the concentration divided by the molar mass ($[A]/M_A$).

The overall mass-transfer coefficient, k_L , is obtained from the following Sherwood relation:³⁸

$$Sh = \frac{k_L d_B}{D_{CO_2}} = 2 + 0.015 Re^{0.89} Sc^{0.7} \quad (28)$$

whereas the enhancement factor is calculated using the relation given by Westerterp et al.:³⁹

$$E = \begin{cases} -\frac{Ha^2}{2(E_\infty - 1)} + \sqrt{\frac{Ha^4}{4(E_\infty - 1)^2} + \frac{E_\infty Ha^2}{E_\infty - 1} + 1} & E_\infty > 1 \\ 1 & E_\infty \leq 1 \end{cases} \quad (29)$$

where

$$E_\infty = \left(1 + \frac{[OH^-] D_{OH^-}}{2 D_{CO_2} H[CO_2(g)]} \right) \sqrt{\frac{D_{CO_2}}{D_{OH^-}}} \quad (30)$$

$$Ha = \frac{\sqrt{k_{11} D_{CO_2} [OH^-]}}{k_L} \quad (31)$$

The solubility of CO_2 in aqueous electrolytic solutions was estimated using the method presented by Weisenberger and Schumpe.⁴⁰

$$\log\left(\frac{H^w}{H}\right) = \sum (h_i + h_g) c_i \quad (32)$$

H^w is the solubility coefficient of CO_2 in pure water and was taken from Versteeg and Van Swaaij:⁴¹

$$H^w = 3.59 \times 10^{-7} R T e^{2044/T} \quad (33)$$

For the parameters h_i and h_g , the interested reader is referred to Weisenberger and Schumpe⁴⁰ or Darmana et al.⁸ c_i is the molar concentration of the corresponding ion or gas.

The diffusivity of CO_2 in pure water, $D_{CO_2}^w$, was taken from Versteeg and Van Swaaij:⁴¹

$$D_{CO_2}^w = 2.35 \times 10^{-6} e^{-2119/T} \quad (34)$$

The diffusion of gases into aqueous electrolyte solutions was estimated by the method suggested by Ratcliff and Holdcroft:⁴²

$$\frac{D_{CO_2}}{D_{CO_2}^w} = 1 - 1.29 \times 10^{-4} [OH^-] \quad (35)$$

3. Numerical Solution Method

All of the numerical simulations are carried out with the commercial CFD package *CFX-4.4* of AEA Technology, Harwell, U.K. The total domain is subdivided into uniform computational grid cells with $\Delta x = \Delta y = \Delta z = 0.01$ m. Equations 1 and 2 are solved in a transient fashion. Different

time steps are used for each of the cases, and these are listed in Table 2. The curvature-compensated convective transport scheme is used for the discretization of all convective terms. "Opening" boundaries are applied at the outlet, which require that

$$\alpha_L = 0; \quad \alpha_G = 1 \quad (36)$$

A gas cap above the liquid-free surface is included in the simulations. In this gas cap, special measures need to be taken to prevent numerical problems due to the high gas volume fraction. This is accomplished as follows:

$$\alpha_L < 0.55 \begin{cases} C_D = 0.05 \\ C_L = 0 \\ C_{VM} = 0 \end{cases} \quad (37)$$

With these measures, eqs 1 and 2 in approximation reduce to those for single-phase flow. A small finite value for C_D is required in eq 37 to guarantee proper coupling of the two phases.

It should also be noted that an unrealistically large bubble size might be obtained from eq 9 when the local bubble number density is very small ($nV_{cell} \ll \varepsilon$, $\varepsilon = 10^{-6}$). To prevent this from happening, a bubble size cutoff is used in our simulation, which takes a value of $d_{B,cutoff} = 4.05$ mm:

$$d_B = \max(d_{B,cutoff}, d_{32}) \quad (38)$$

4. Physical Problem

A sketch of the bubble column studied in this work is shown in Figure 3. The column is initially filled to a height of 0.45 m with quiescent pure water or an aqueous NaOH solution with an initial pH value of 12. Air or pure CO_2 is used as the dispersed gas phase and injected into the center of the bottom plane with $A_{in} = 0.03 \times 0.03$ m² and $V_{G,in} = 0.1225$ m s⁻¹ corresponding to a superficial gas velocity of 4.9 mm s⁻¹. The inlet gas volume fraction and bubble number density were chosen as $\alpha_{G,in} = 1.0$ and $n_{in} = 2.98 \times 10^7$, resulting in an inlet bubble size of 4 mm, following from eq 9. Initially, the gas cap above the liquid is filled with inert N_2 gas. The gas-liquid flow is assumed to be homogeneous (bubbly) flow, and breakup and coalescence are not accounted for. The width, depth, and height of the column are respectively set to $W = 0.15$ m, $D = 0.15$ m, and $H = 0.55$ m. No slip conditions were applied on the confining walls, whereas a pressure boundary was applied at the outlet of the column.

All of the remaining simulation parameters and physical properties are presented in Table 2. Diffusivities of the four species were obtained from the work of Bauer.³⁸ An initial bubble size of 4 mm is used, and the bubble number density equation is incorporated to obtain the bubble size, which is used to calculate the interfacial closure coefficients and the overall mass-transfer coefficient.

5. Results and Discussion

The implementation of the number density model in *CFX-4.4* is first tested with the aid of a case without absorption. Subsequently, the model is applied to the cases of physical absorption of pure CO_2 into pure water and chemisorption of pure CO_2 into an aqueous NaOH solution with an initial pH value of 12.

5.1. No Absorption. Case 1 is employed to verify the implementation of the bubble number density model in *CFX-4.4*. In this case, a constant bubble diameter and drag coefficient ($C_D = 1.071$) are assumed and the Sauter mean diameter is

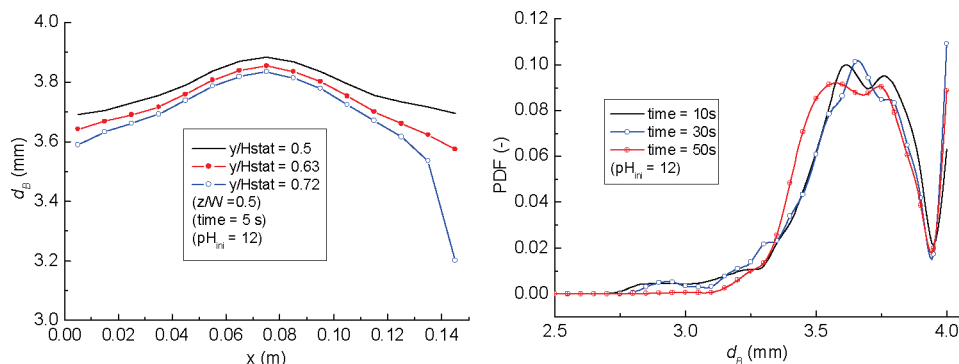


Figure 14. Instantaneous bubble size distribution in the horizontal direction at different heights (left) and entire column-averaged bubble size distribution at different times (right) during chemisorption of pure CO_2 in an aqueous NaOH solution with an initial pH of 12. A bubble number density equation is used to obtain the bubble size (case 5).

obtained through eq 9 and compared to the bubble size used at the inlet (i.e., $d_{B,in} = 4$ mm). In this case, there is no sink term in the gas-phase continuity equation (eq 1). Hence, it has the same form as the bubble number density equation (eq 8). When the values obtained for α_G and n are substituted in eq 9, a constant bubble size equal to the inlet bubble size is expected. Figure 4 shows the predicted local bubble diameter history at a monitoring point in the center of the column. Clearly, an almost constant bubble size is achieved in this case; i.e., the error in the predicted bubble diameter is less than 0.1%. Figure 5 presents the simulated instantaneous bubble diameter in horizontal and vertical directions. It is found here that the predicted bubble diameter is consistent with the assumed bubble diameter, which proves that the bubble number density equation has been implemented correctly.

5.2. Physical Absorption of Pure CO_2 Bubbles in Water. During physical absorption of pure CO_2 in water, dispersed CO_2 bubbles are shrinking. A number density equation is solved here to keep track of the bubble size change in order to couple the mass transfer and flow dynamics. The bubble diameter obtained from eq 9 is used to calculate the drag coefficient (eq 16), bubble-induced turbulence (eq 7), and mass-transfer rate (eq 26). Figure 6 displays the instantaneous predicted bubble diameter in horizontal and vertical directions. It is seen that vertically the bubble diameter shrinks from 4 to about 3.6 mm because of physical absorption. Along the column walls, the bubble residence time is longer than that in the center of the bubble column, leading to a smaller bubble diameter in those regions.

Figure 7 illustrates the instantaneous bubble size distribution and liquid-phase velocity field. As expected, the flow in the column is quite dynamic, and the bubble size is decreasing with increasing distance from the sparger. As found earlier, the bubble size along the confining walls is relatively small.

Figure 8 demonstrates the probability distribution function of the bubble size averaged in the entire column at different times. As expected, with time the liquid gets saturated with $CO_2(aq)$ and reduction in the bubble size is less. Hence, the bubble size distribution in the entire column is shifting toward larger bubble sizes. Because of the small and large scales of mixing induced by convection and the meandering behavior of the bubble plume, the local bubble size increasing behavior shows an oscillatory behavior, which is shown in Figure 9.

A comparison of the overall normalized dissolved CO_2 concentration of the entire column obtained from the constant bubble size (case 4) and dynamic bubble size (case 3) has also been made and is displayed in Figure 10. In case 3, the bubble size decreases because of mass transfer, which leads to a longer

residence time, and thus the predicted dissolved CO_2 concentration is a little bit higher than that from case 4, where a constant bubble size is used.

The results of both models are also compared with those obtained with a simple macroscopic model. In this model, ideal mixing of the liquid phase is assumed and the gas fraction and average bubble size resulting from case 3 are used as input parameters. As the macroscopic model is fed with data from case 3, the results of the simple model and the complete model for case 3 agree rather well. The discrepancy between the macroscopic model (see Darmana et al.⁸) and cases 3 and 4 comes from the fact that, in the detailed model, the gas volume fraction and bubble size are changing with time.

5.3. Chemisorption of Pure CO_2 Bubbles in an Aqueous NaOH Solution. In this section, we study the chemisorption of pure CO_2 in an aqueous NaOH solution with an initial pH value of 12. Transport equations for the mass fractions of aqueous CO_2 , OH^- , HCO_3^- , and CO_3^{2-} as well as the mass fraction of CO_2 in the gas phase are solved.

Because the chemisorption of CO_2 is characterized by the consumption of CO_2 and OH^- as well as the production of CO_3^{2-} , Figure 11 shows the evolution of the local bubble diameter and the instantaneous species concentration of OH^- and CO_3^{2-} at a monitoring point. It is observed here that the bubble size decreases dramatically shortly after CO_2 bubbles arrive at the monitoring point. Subsequently, OH^- is consumed immediately to form CO_3^{2-} . Then, the local bubble size is rather constant for a short period because the local gas holdup is also constant. Because of the consumption of CO_2 and the subsequent meandering behavior of the bubble plume, the bubble size history shows an oscillating pattern, which leads to an oscillatory decrease of the OH^- concentration.

In Figure 12, the predicted histories of pH and the CO_3^{2-} species concentration averaged over the entire column obtained from cases 4 and 5 are compared with those obtained from the simple macroscopic model.⁸ It is found that there is a significant difference between cases 4 and 5, which implies that it is important to use a dynamic bubble size.

Figure 13 displays snapshots for bubble size and gas-phase velocity field, liquid-phase volume fraction, and velocity field and pH distribution in the column. As found in Figure 13, the bubble size distribution greatly depends on the local flow structure. Furthermore, the bubble size change is still within 1 mm, which is caused by the short residence time of bubbles. After 40 s, the pH is distributed uniformly around a value of about 9.2, which is due to the fact that the reactive system has passed the first acidity constant of $pK_{a,1} = 10.3$.

Figure 14 shows the instantaneous predicted bubble diameter in the horizontal direction at different heights and the variation of the entire column bubble size distribution with time. It is found again that, in the beginning, the bubble size decreases with increasing height. Furthermore, the bubble diameter in the column center is larger than that along the walls because of differences in residence times. Contrary to the case of physical absorption, the bubble size distribution hardly changes with time. This can be explained by the fact that all transferred CO_2 immediately reacts, leading to an approximately constant driving force for mass transfer and the associated mass-transfer rate.

6. Conclusions

Numerical simulations of the gas–liquid two-phase flow with mass transfer in a square cross-sectioned bubble column were carried out, by incorporating a bubble number density equation. First, a simulation without mass transfer was carried out to verify that the bubble size that follows from this equation is the same as the assumed bubble size. The error in the predicted bubble size was less than 0.1%, which makes the model suited for application to systems with mass transfer.

When pure CO_2 is absorbed into water, the flow is quite dynamic, and the bubble size does not change much; bubble sizes range from 3 to 4 mm in the entire column. Generally, the bubble size inside the bubble plume is larger than those close to the walls, where the bubbles that are trapped in a strong downflow have more time to transfer species.

Chemisorption of pure CO_2 into an aqueous NaOH solution with an initial pH value of 12 has been simulated as well. Full coupling of fluid flow, mass transfer, and chemical reaction is achieved by employing the bubble number density model. Because the mass transfer is not chemically enhanced ($E = 1$), the bubble size ranges from 2.7 to 4 mm in this test case. The simulated column-averaged pH agrees well with that obtained from a simple macroscopic model.⁸ The differences between the macroscopic model and the numerical results obtained with a constant bubble size are due to the decoupling of fluid flow and mass transfer in the latter model. This indicates the necessity to account for changes in the bubble size and proves the added value of the bubble number density equation.

All of the numerical results are only presented qualitatively; a more detailed comparison of the E–E results with available E–L simulated results and/or experimental data is still required. Also, numerical simulation of chemisorption of pure CO_2 in a NaOH solution with higher pH should be carried out.

Appendix A: Kinetics

The forward rate constant k_{11} of eq 18 is calculated via the relation presented by Pohorecki and Moniuk:⁴³

$$\log\left(\frac{k_{11}}{k_{11}^\infty}\right) = 0.221I - 0.016I^2 \quad (\text{A1})$$

where the reaction rate constant at an infinitely diluted solution ($\text{m}^3 \text{ kmol}^{-1} \text{ s}^{-1}$) is given by

$$\log(k_{11}^\infty) = 11.895 - \frac{2382}{T} \quad (\text{A2})$$

This equation is valid in the temperature range of 291–314 K.

The ionic strength, I , is calculated as

$$I = \frac{1}{2}([Na^+]Z_{Na^+}^2 + [OH^-]Z_{OH^-}^2 + [HCO_3^-]Z_{HCO_3^-}^2 + [CO_3^{2-}]Z_{CO_3^{2-}}^2) \quad (\text{A3})$$

where $z_{Na^+} = 1$, $z_{OH^-} = -1$, $z_{HCO_3^-} = -1$, and $z_{CO_3^{2-}} = -2$.

The backward rate constant k_{12} (s^{-1}) is calculated via the equilibrium constant K_3 and K_w . K_3 is calculated according to Edwards et al.:⁴⁴

$$K_3 = \frac{[HCO_3^-][H^+]}{[CO_2]} = \exp\left(\frac{-12092.1}{T} - 36.786 \ln(T) + 235.482\right) \quad (\text{A4})$$

The solubility product, K_w , was taken from Tsonopoulos et al.:⁴⁵

$$K_w = [H^+][OH^-] = 10^{1-5839.5/T+22.4773\log(T)-61.20621} \quad (\text{A5})$$

The backward reaction is then obtained using the following relation:

$$K_1 = \frac{k_{11}}{k_{12}} = \frac{K_3}{K_w} \quad (\text{A6})$$

Because the second reaction involves a proton transfer, it is very rapid. Eigen⁴⁶ determined the rates of reactions involving protons or hydroxyl ions in an aqueous solution to be on the order of 10^{10} – $10^{11} \text{ m}^3 \text{ kmol}^{-1} \text{ s}^{-1}$. The backward reaction rate k_{22} (s^{-1}) is calculated using the equilibrium constant K_2 ($\text{m}^3 \text{ kmol}^{-1}$), as suggested by Hikita et al.:⁴⁷

$$K_2 = \frac{k_{21}}{k_{22}} \quad (\text{A7})$$

with

$$\log K_2 = \log K_2^\infty + \frac{1.01\sqrt{[Na^+]}}{1 + 1.27\sqrt{[Na^+]}} + 0.125[Na^+] \quad (\text{A8})$$

where

$$\log K_2^\infty = \frac{1568.94}{T} + 0.4134 - 0.00673T \quad (\text{A9})$$

Nomenclature

- a = interfacial area (m^2); strain rate (s^{-1})
- B = subgrid-scale model parameter ($\text{m}^4 \text{ s}^{-4}$)
- d = diameter (m)
- c = species concentration (kmol m^{-3})
- C = model coefficient
- D = depth (m); diffusivity ($\text{m}^2 \text{ s}^{-1}$)
- g = gravitational constant (m s^{-1})
- E = enhancement factor
- E_b = bubble height over width ratio
- $E\ddot{o}$ = Eötvös number
- H = Henry's constant; height (m)
- Ha = Hatta number
- I = ionic concentration (kmol m^{-3})
- k_{11} = forward reaction rate constant ($\text{m}^3 \text{ kmol}^{-1} \text{ s}^{-1}$)
- k_{12} = backward reaction rate constant (s^{-1})
- k_{21} = forward reaction rate constant ($\text{m}^3 \text{ kmol}^{-1} \text{ s}^{-1}$)
- k_{22} = backward reaction rate constant (s^{-1})
- k_f = overall mass transfer coefficient (m s^{-1})
- K_1 = equilibrium constant for reaction 1 ($\text{m}^3 \text{ kmol}^{-1}$)
- K_2 = equilibrium constant for reaction 2 ($\text{m}^3 \text{ kmol}^{-1}$)
- \mathbf{M} = interfacial force (kg m s^{-2})
- \dot{m} = mass transfer from gas (single bubble) (kg s^{-1})
- m = mass of a single bubble (kg)
- n = bubble number density (m^{-3})
- P = pressure (N m^{-2})

PDF = probability distribution function

R = reaction rate ($\text{kmol m}^{-3} \text{s}^{-1}$)

Re = Reynolds number

S = source term in the species balance equation ($\text{kg m}^{-3} \text{s}^{-1}$)

Sh = Sherwood number

t = time (s)

T = temperature (K)

\mathbf{u} = velocity vector (m s^{-1})

u = velocity component in the x direction (m s^{-1})

v = slip velocity (m s^{-1})

v = velocity component in the y direction (m s^{-1})

w = velocity component in the z direction (m s^{-1})

Y = mass fraction

z = ionic charge

$[\]$ = concentration (kmol m^{-3})

Greek Letters

Δ = subgrid length scale (m)

Γ = species diffusion coefficient ($\text{m}^2 \text{s}^{-1}$)

ρ = density (kg m^{-3})

β = subgrid-scale model parameter ($\text{m}^2 \text{s}^{-2}$)

σ = interfacial tension (N m^{-1})

μ = viscosity ($\text{kg m}^{-1} \text{s}^{-1}$)

τ = stress tensor (N m^{-2})

Subscripts

aq = aqueous

B = bubble

BIT = bubble-induced turbulence

D = drag

e = equilibrium

eff = effective

G = gas

GL = gas–liquid

h = horizontal direction

i = Cartesian ordinate direction index

j = Cartesian ordinate direction index

k = phase indicator

L = lift, liquid

Lam = laminar

rel = relative velocity

S = subgrid-scale model

Tur = shear-induced turbulence

v = vertical direction

VM = virtual mass

32 = Sauter mean diameter

Superscript

w = water

Literature Cited

- (1) Vreman, A. W. An eddy-viscosity subgrid-scale model for turbulent shear flow: Algebraic theory and applications. *Phys. Fluids* **2004**, *16*, 3670.
- (2) Becker, S.; Sokolichin, A.; Eigenberger, G. Gas–liquid flow in bubble columns and loop reactors: Part II. Comparison of detailed experiments and flow simulations. *Chem. Eng. Sci.* **1994**, *49*, 5747.
- (3) Deen, N. G.; Solberg, T.; Hjertager, B. H. Large eddy simulation of the gas–liquid flow in a square cross-sectioned bubble column. *Chem. Eng. Sci.* **2001**, *56*, 6341.
- (4) Milelli, M.; Smith, B. L.; Lakehal, D. In Large-eddy simulation of turbulent shear flows laden with bubbles. *Direct and Large-Eddy Simulation IV*; Geurts, B. J., Friedrich, R., Metais, O., Eds.; Kluwer Academic Publishers: Amsterdam, The Netherlands, 2001; p 461.
- (5) Dhotre, M. T.; Niceno, B.; Smith, B. L. Large eddy simulation of a bubble column using dynamic sub-grid scale model. *Chem. Eng. J.* **2008**, *136* (2–3), 337.
- (6) Delnoij, E.; Kuipers, J. A. M.; Van Swaaij, W. P. M. Dynamic simulation of gas–liquid two-phase flow: effect of column aspect ratio on the flow structure. *Chem. Eng. Sci.* **1997**, *52*, 3759.
- (7) Delnoij, E.; Kuipers, J. A. M.; Van Swaaij, W. P. M. A three-dimensional model for gas–liquid bubble columns. *Chem. Eng. Sci.* **1999**, *54*, 2217.
- (8) Darmana, D.; Deen, N. G.; Kuipers, J. A. M. Detailed modeling of hydrodynamics, mass transfer and chemical reactions in a bubble column using a discrete bubble model. *Chem. Eng. Sci.* **2005**, *60*, 3383.
- (9) Zhang, D.; Deen, N. G.; Kuipers, J. A. M. Numerical simulation of dynamic flow behavior in a bubble column: A study of closures for turbulence and interface forces. *Chem. Eng. Sci.* **2006**, *61*, 7593.
- (10) Lo, S. *Application of Population Balance to CFD Modelling of Bubbly Flow via the MUSIG model*; AEA Technology: Harwell, U.K., 1996; AEAT-1096.
- (11) Wu, Q.; Kim, S.; Ishii, M.; Beus, S. G. One-group interfacial area transport in vertical bubbly flow. *Int. J. Heat Mass Transfer* **1998**, *41*, 1103.
- (12) Ishii, M.; Kim, S. Micro four-sensor probe measurement of interfacial area transport for bubbly flow in round pipes. *Nucl. Eng. Des.* **2001**, *205*, 123.
- (13) Yao, W.; Morel, C. Volumetric interfacial area prediction in upward bubbly two-phase flow one-group interfacial area transport in vertical bubbly flow. *Int. J. Heat Mass Transfer* **2004**, *47*, 307.
- (14) Ishii, M.; Kim, S.; Kelly, J. Development of interfacial area transport equation. *Nucl. Eng. Technol.* **2005**, *37*, 525.
- (15) Lo, S.; Rao, P. Modelling of droplet breakup and coalescence in an oil-water pipeline. *Proceedings of the 6th International Conference on Multiphase Flow*, Leipzig, Germany, July 9–13, 2007.
- (16) Fleischer, C.; Becker, S.; Eigenberger, G. Detailed modeling of the chemisorption of CO_2 into NaOH in a bubble column. *Chem. Eng. Sci.* **1996**, *51*, 1715.
- (17) Márquez, M. A.; Amend, R. J.; Carbonell, R. G.; Sáez, A. E.; Roberts, G. W. Hydrodynamics of gas-lift reactors with a fast, liquid-phase reaction. *Chem. Eng. Sci.* **1999**, *54*, 2263.
- (18) Márquez, M. A.; Sáez, A. E.; Carbonell, R. G.; Roberts, G. W. Coupling of hydrodynamics and chemical reaction in gas-lift reactors. *AIChE J.* **1999**, *45*, 410.
- (19) Bauer, M.; Eigenberger, G. A concept for multi-scale modeling of bubble columns and loop reactors. *Chem. Eng. Sci.* **1999**, *54*, 5109.
- (20) Bauer, M.; Eigenberger, G. Multiscale modeling of hydrodynamics, mass transfer and reaction in bubble columns reactors. *Chem. Eng. Sci.* **2001**, *56*, 1067.
- (21) Rigopoulos, S.; Jones, A. A hybrid CFD-reaction engineering framework for multiphase reactor modeling: basic concept and application to bubble column reactors. *Chem. Eng. Sci.* **2003**, *58*, 3077.
- (22) Zhang, D.; Deen, N. G.; Kuipers, J. A. M. Numerical Modeling of Hydrodynamics, Mass transfer and Chemical Reaction in Bubble Columns. *Proceedings of the 6th International Conference on Multiphase Flow*, Leipzig, Germany, July 9–13, 2007.
- (23) Ishii, M. Two-fluid model for two-phase flow. *Multiphase Sci. Technol.* **1990**, *5*, 1–58.
- (24) Millies, M.; Mewes, D. Interfacial area density in bubbly flow. *Chem. Eng. Proc.* **1999**, *38*, 307.
- (25) Hibiki, T.; Ishii, M. One-group interfacial area transport of bubbly flow in vertical round tubes. *Int. J. Heat Mass Transfer* **2000**, *43*, 2711.
- (26) Lehr, F.; Mewes, D. A transport equation for the interfacial area density applied to bubble columns. *Chem. Eng. Sci.* **2001**, *56*, 1159.
- (27) Ishii, M.; Kim, S.; Uhle, J. Interfacial area transport equation: One-group interfacial area transport model development and benchmark experiments. *Int. J. Heat Mass Transfer* **2002**, *45*, 3111.
- (28) Kim, S.; Ishii, M.; Sun, X.; Beus, S. G. Interfacial area transport and evaluation of source terms for confined air-water bubbly flow. *Nucl. Eng. Des.* **2002**, *219*, 61.
- (29) Yeoh, G. H.; Tu, J. Y. Modeling gas–liquid bubbly flows. *Proceedings of the 15th Australasian Fluid Mechanics Conference*, University of Sydney, Sydney, Australia, Dec 13–17, 2004.
- (30) Drew, D. A.; Passman, S. L. Theory of multicomponent fluids. *Appl. Math. Sci.* **1999**, 135.
- (31) Jakobsen, H. A.; Sannæs, B. H.; Grevskott, S.; Svendsen, H. F. Modeling of vertical bubble-driven flows. *Ind. Eng. Chem. Res.* **1997**, *36*, 4052.
- (32) Zhang, D. Eulerian modeling of reactive gas–liquid flow in a bubble column. Ph.D. Thesis, University of Twente, Enschede, The Netherlands, 2007.
- (33) Sato, Y.; Sekoguchi, K. Liquid velocity distribution in two-phase bubble flow. *Int. J. Multiphase Flow* **1975**, *2*, 79.
- (34) Bove, S.; Solberg, T.; Hjertager, B. H. A novel algorithm for solving population balance equations: the parallel parent and daughter classes. Derivation, analysis and testing. *Chem. Eng. Sci.* **2005**, *60*, 1449.
- (35) Dorao, C. A.; Jakobsen, H. A. A least squares method for the solution of population balance problems. *Comput. Chem. Eng.* **2006**, *30*, 535.

- (36) Tomiyama, A. Drag, lift and virtual mass forces acting on a single bubble. *3rd International Symposium on Two-Phase Flow Modeling and Experimentation*, Pisa, Italy, Sept 22–24, 2004.
- (37) Dijkhuizen, W.; Van den Hengel, E. I. V.; Deen, N. G.; Van Sint Annaland, M.; Kuipers, J. A. M. Numerical investigation of closures for interface forces acting on single air-bubbles in water using Volume of Fluid and Front Tracking models. *Chem. Eng. Sci.* **2005**, *60*, 6169.
- (38) Bauer, M. On the multiscale modeling of bubble column reactors. Ph.D. Thesis, University of Stuttgart, Stuttgart, Germany, 2001.
- (39) Westerterp, K. R.; Van Swaaij, W. P. M.; Beenackers, A. A. C. M. *Chemical Reactor Design and Operation*; John Wiley & Sons Ltd.: New York, 1984; p 411.
- (40) Weisenberger, S.; Schumpe, A. Estimation of gas solubility in salt solutions at temperatures from 273 to 363 K. *AIChE J.* **1996**, *42*, 298.
- (41) Versteeg, G. F.; Van Swaaij, W. P. M. Solubility and diffusivity of acid gases (CO₂ and N₂O) in aqueous alkaloamine solutions. *J. Chem. Eng. Data* **1988**, *33*, 29.
- (42) Ratcliff, G. A.; Holdcroft, J. G. Diffusivities of gases in aqueous electrolyte solutions. *Trans. Inst. Chem. Eng.* **1963**, *41*, 315.
- (43) Pohorecki, R.; Moniuk, W. Kinetics of reaction between carbon dioxide and hydroxyl ions in aqueous electrolytic solutions. *Chem. Eng. Sci.* **1988**, *43*, 1677.
- (44) Edwards, T. J.; Maurer, G.; Newman, J.; Prausnitz, J. M. Vapor–liquid equilibrium in multicomponent aqueous solutions of volatile weak electrolytes. *AIChE J.* **1978**, *24*, 966.
- (45) Tsonopoulos, C.; Coulson, D. M.; Inman, L. W. Ionization constants of water pollutants. *J. Chem. Eng. Data* **1976**, *21*, 190.
- (46) Eigen, M. Method for investigation of ionic reactions in aqueous solutions with half times as short as 10^{−9} sec. *Discuss. Faraday Soc.* **1954**, *17*, 194.
- (47) Hikita, H.; Asai, S.; Takatsuka, T. Absorption of carbon dioxide into aqueous sodium hydroxide and sodium carbonate–bicarbonate solutions. *Chem. Eng. J.* **1976**, *11*, 131.

Received for review February 8, 2008
 Revised manuscript received April 7, 2008
 Accepted May 6, 2008

IE800233Y